Journal of Power Sources 261 (2014) 292–305

Contents lists available at ScienceDirect

Journal of Power Sources

journal homepage: www.elsevier.com/locate/jpowsour

Robust DC/DC converter control for polymer electrolyte membrane fuel cell application

Ya-Xiong Wang [a], Duck-Hyun Yu [a], Shi-An Chen [a,b], Young-Bae Kim [a,*]

[a] Department of Mechanical Engineering, Chonnam National University, Gwangju, Republic of Korea
[b] School of Automotive and Traffic Engineering, Jiangsu University, Zhenjiang, China

HIGHLIGHTS

- Robust controller is designed to enhance the PEMFC-fed DC/DC converter output.
- Simple and accurate control-oriented fuel cell and DC/DC converter model is developed.
- Simulation and experimental validations are performed to show TDC's control efficacy.

GRAPHICAL ABSTRACT

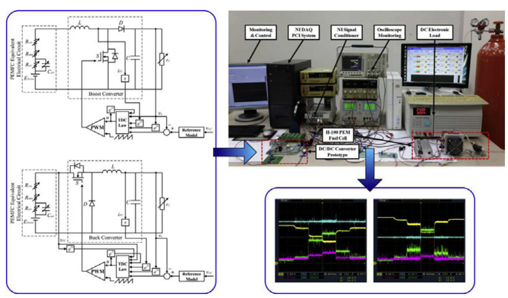

ARTICLE INFO

Article history:
Received 3 January 2014
Received in revised form
13 March 2014
Accepted 14 March 2014
Available online 28 March 2014

Keywords:
Control-oriented polymer electrolyte membrane fuel cell dynamic model
Boost converter
Buck converter
Model predictive control
Time delay control

ABSTRACT

This study investigates a robust controller in regulating the pulse width modulation (PWM) of a DC/DC converter for a polymer electrolyte membrane fuel cell (PEMFC) application. A significant variation in the output voltage of a PEMFC depends on the power requirement and prevents a PEMFC from directly connecting to a subsequent power bus. DC/DC converters are utilized to step-up or step-down voltage to match the subsequent power bus voltage. In this study, a full dynamic model, which includes a PEMFC and boost and buck DC/DC converters, is developed under MATLAB/Simulink environment for control. A robust PWM duty ratio control for the converters is designed using time delay control (TDC). This control enables state variables to accurately follow the dynamics of a reference model using time-delayed information of plant input and output information within a few sampling periods. To prove the superiority of the TDC performance, traditional proportional-integral control (PIC) and model predictive control (MPC) are designed and implemented, and the simulation results are compared. The efficacies of TDC for the PEMFC-fed PWM DC/DC converters are validated through experimental test results using a 100 W PEMFC as well as boost and buck DC/DC converters.

1. Introduction

Fuel cell is a potential clean energy solution to remedy the increasing environmental pollution issues, and the polymer electrolyte membrane fuel cell (PEMFC) shows superiority in the automobile industry [1–3]. The PEMFC exhibits higher efficiency, lower or zero emission, lower noise, and lower operation temperature compared with other types of fuel cells. For vehicular application, a regulated output voltage of PEMFC is compulsory to feed the power for the subsequent electrical motor system; however, the output voltage of a PEMFC is not constant because of the characteristic of its polarization curve, which is governed by an electrochemical reaction. The electrochemical reaction is affected by variations in the operating points of parameters such as mass flow

* Corresponding author. Tel.: +82 62 5301677.
E-mail address: ybkim@chonnam.ac.kr (Y.-B. Kim).

http://dx.doi.org/10.1016/j.jpowsour.2014.03.048
0378-7753/

rate, inlet pressure, stack temperature, water content, relative humidity, stoichiometry of air and hydrogen, and channel geometry [4–10]. Moreover, recent power buses for fuel cell hybrid vehicles require different dual voltage links, namely, higher and lower links. A higher link of 24 V is used for electric motors, air-conditioners, and pump connections, whereas the lower link of 12 V is used for conventional switches and lamp connections [3]. Therefore, DC/DC converters are the best choice for regulating the output voltage of PEMFC to satisfy this dual power bus requirement. Additionally, DC/DC converters can step-up or step-down input voltage depending on the different operating conditions, i.e., boost converter for high voltage (step-up voltage) [8,11,12] and buck converter for low voltage (step-down voltage) [13,14]. Thus, PEMFC-fed DC/DC converter system can be regarded as a typical integrated power supply system (Fig. 1) that can constantly supply the desired DC link power.

Controlling the integrated power system exhibits challenging problems because PEMFC and DC/DC converters are non-linear systems resulting in coupled characteristics. To control the integrated system, the construction of a simple and accurate control-oriented dynamic model is necessary. Choe et al. [8] developed an associated PEMFC pulse width modulation (PWM) DC/DC converter model by considering balance-of-plant (BOP) of a PEMFC, including air supply and thermal systems, and a DC/DC boost converter. This model showed comprehensive control variables with high-order dynamics and a complex control process validated only by simulation results. A more detailed PEMFC model for employing DC/DC converter can be found in Refs. [15,39]. To simplify the modeling process and reduce computational burden for real-time control implementation, Bjazic et al. [11] and Shtessel et al. [22] presented equivalent electrical circuit dynamic models of a PEMFC, which were subsequently used in a DC/DC boost converter with a double layer capacitor to simulate the electrode behavior of a PEMFC system [16]. A modified equivalent electrical circuit approach with variable capacitance was implemented in Ref. [12].

An accurate and robust PWM duty ratio control is required to manipulate output voltage that precisely tracks the setpoint value, because DC/DC converters are inherently non-linear with variations in system parameters. Numerous studies have reported on the accurate and robust PWM duty ratio control for DC/DC converter. Traditional small signal state-space averaging method was first summarized in Ref. [17]. This method is widely used for the linearization power converter to construct linear feedback control systems, such as linear quadratic regulator control [18] and proportional-integral (PI) or proportional-integral-derivative control [8,12,19]. However, the linear control of DC/DC converter is not suitable for PEMFC application because the PEMFC operation point is always varying compared with the normal DC power source. Many robust control approaches, such as H_∞ control [20], gain-scheduled control [21], and sliding mode control (SMC), have recently been developed to cope with non-linearity and ensure stability [13,22–25]. Moreover, several complicated control techniques have been introduced to improve the DC/DC converter performance. Wai et al. [26] presented a total SMC with adaptive linear neural network filter to reduce current ripple to protect clean-energy sources. Geyer et al. [27] introduced a model predictive control (MPC) based on hybrid piecewise affine model approximations to efficiently reject disturbances inherent in the input voltage. Similar results were collected in Ref. [28], in which five techniques from hybrid and optimal control were evaluated and compared to diminish the converter output voltage ripples under variations in supply voltage and load resistor. The dynamic evolution control for fuel cell-based DC/DC converter that satisfies the desired performance was developed in Ref. [29]. Optimization algorithms such as neural network (NN) [30] and genetic algorithm [31] have also been reported to tune the control parameters to improve DC/DC converter control performance.

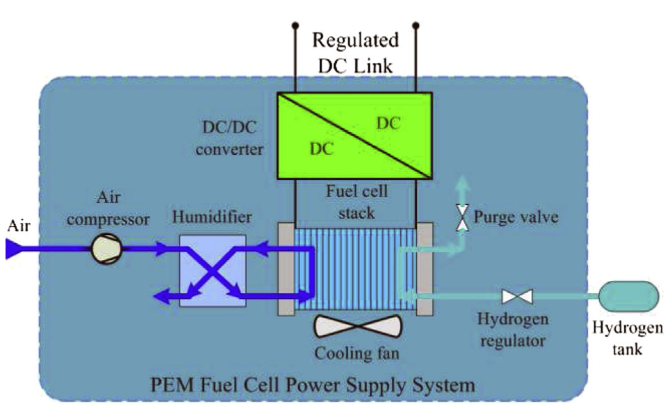

Fig. 1. PEMFC integrated power supply system.

This study presents a new design methodology of time delay control (TDC) for the PEMFC-fed PWM boost and buck DC/DC converter control. TDC is a totally different control algorithm from the widely used robust control concepts, such as SMC and NN, because it is based on the model reference control. TDC was originally proposed by Youcef-Toumi et al. [32]. The prominent advantage of TDC is its ability to represent unknown system dynamics or disturbance using the time-delayed information of plant input and output relation just within several sampling periods. TDC control system structure, stability, controllability, and observability have been discussed in some studies [33,34]. Moreover, TDC has been widely applied in various industrial areas, such as robot manipulation control [35], PEMFC air supply system implementation [15,36], and boost converter control [37].

In the present study, an integrated system dynamic model is derived in Section 2, where an equivalent electrical circuit with variable double-layer capacitor is introduced to replace PEMFC dynamic characteristic. TDC is utilized to design the DC/DC converter PWM duty ratio controller in Section 3. In Section 3, two conventional control methods, namely, PIC and MPC, are performed on the same platform to show the superiority of TDC. Simulation results of the designed PEMFC-fed PWM DC/DC converters are expressed in Section 4. To validate the efficacy of TDC, experiments based on boost and buck DC/DC converters with commercial PEMFC *Horizon* H-100 with *National Instrument* (NI) DAQ PCI board for real-time control are performed, and the results are also presented in this section.

2. PEMFC-based DC/DC converter model

PEMFC-based DC/DC converter model requires the internal relation between PEMFC and DC/DC converter because the output voltage of PEMFC is the supply voltage of the DC/DC converter. Therefore, the development of a full control-oriented model including PEMFC and DC/DC converters is necessary. The highest accuracy of PEMFC model can be obtained from a CFD-based model with numerous state variables [6,10] or from a comprehensive BOP-based model [15]. However, these approaches cannot be fully managed in practice because of the large amount of highly coupled variables. Therefore, these approaches are not suitable for control. The major characteristic of PEMFC is indicated by its polarization curve, which intuitively shows the PEMFC output voltage versus

stack current density relation. Therefore, equivalent electrical circuit models with variable double-layer capacitor can be used in our study to control the PEMFC electrochemical transient characteristics. This model can facilitate controller design with high accuracy and small number of state variable. The validation of a developed PEMFC model is proven by comparing the test results obtained from *Horizon* H-100, a commercial PEMFC, which comprised 20 cells with 100 W rated power [38]. H-100 is a convenient and delicate PEMFC that is air blown and cooled by an integrated fan, supplied with hydrogen, purged by two valves, and equipped with self-humidification. Thus, it is suitable for low-power system application.

2.1. PEMFC model

The principle of PEMFC reaction involves the transport of hydrogen to the anode catalyst layer and its split into protons and electrons under a defined pressure. The membrane can transfer protons only to the cathode, but it can stop electrons. Subsequently, electrons generate electricity through an external electrical circuit. Protons, oxygen, and electrons react to produce water and heat at the cathode. The output voltage of the single cell is described by [9]

$$V_{\text{cell}} = E_{\text{Nernst}} - V_{\text{act}} - V_{\text{ohm}} - V_{\text{con}} \tag{1}$$

where E_{Nernst} is the reversible voltage, V_{act} is the activation drop, V_{ohm} is the ohmic drop, and V_{con} is the concentration drop. The reversible voltage is calculated by Nernst potential equation [13]. Its value depends on operation temperature and pressure. For a standard condition ($T_0 = 298.15$ K, $P_0 = 101{,}325$ Pa), the standard reversible voltage is 1.229 V [15]. Then, the Nernst potential equation can be written as

$$E_{\text{Nernst}} = 1.229 - 0.85 \times 10^{-3}(T - 298.15) + 4.3085 \times 10^{-5}\left[\ln\left(\frac{P_{H_2}}{101325}\right) + \frac{1}{2}\ln\left(\frac{P_{O_2}}{101325}\right)\right] \tag{2}$$

Based on the simplified parametric equivalent of the general Butler–Volmer equation, the activation drop is given by [12,13]

$$V_{\text{act}} = -[\xi_1 + \xi_2 \cdot T + \xi_3 \cdot T\ln(C_{O_2}) + \xi_4 \cdot T\ln(i_{\text{FC}})] \tag{3}$$

where i_{FC} is the fuel cell current, and ξ_1, ξ_2, ξ_3, and ξ_4 are the cell parametric coefficients, the values of which are identified by experimental fitting. C_{O_2} represents the concentration of oxygen dissolved at the cathode catalytic interface and is calculated by

$$C_{O_2} = \frac{\frac{P_{O_2}}{101{,}325}}{5.08 \times 10^6 \exp\left(-\frac{498}{T}\right)} \tag{4}$$

The ohmic loss caused by the resistance of proton conduction through the membrane and electron transfer through the electrodes is given by [8,9]

$$V_{\text{ohm}} = i_{\text{FC}}(R_{\text{M}} + R_{\text{C}}) \tag{5}$$

where the equivalent resistance of electron transfer R_{C}, is usually considered as a constant value. R_{M} represents the resistance of proton conduction obtained by

$$R_{\text{M}} = \frac{\rho_{\text{M}} \cdot l}{A} \tag{6}$$

where ρ_{M} is the specific resistivity denoted by [9]

$$\rho_{\text{M}} = \frac{181.6\left[1 + 0.03\left(\frac{i_{\text{FC}}}{A}\right) + 0.062\left(\frac{T}{303}\right)^2\left(\frac{i_{\text{FC}}}{A}\right)^{2.5}\right]}{\left[\lambda_{\text{m}} - 0.634 - 3\left(\frac{i_{\text{FC}}}{A}\right)\right]\exp\left[4.18\left(T - \frac{303}{T}\right)\right]} \tag{7}$$

where l and A are the membrane thickness and cell active area, respectively. λ_{m} is the average water content in the membrane, which is based from the membrane humidity [8].

The last term of Eq. (1) corresponds to the concentration loss V_{con}, caused by the insufficient reactant delivery when the current density occurs and is given by [16]

$$V_{\text{con}} = -\frac{RT}{2F} ln\left(1 - \frac{j}{j_{\max}}\right) \tag{8}$$

where j is fuel cell current density defined by

$$j = \frac{i_{\text{FC}}}{A} \tag{9}$$

The electrochemical transient characteristics of PEMFC can be simulated by an equivalent electrical circuit, which is based on the double-layer capacitor charging effect. This effect results in the output voltage with a small time lag when the current suddenly changes. This phenomenon is precisely represented using the first-order time constant made by the capacitor in the activation and concentration polarization [8,16]. The modified equivalent circuit with variable capacitor model [13] is utilized in this study because it exhibits better experimental fitting performance. Fig. 2 shows the equivalent electrical circuit of a PEMFC dynamic model, and the equivalent capacitance is determined by

$$C_{\text{act}} = \frac{1}{\xi_5 \cdot R_{\text{act}}} \tag{10}$$

where ξ_5 is a constant value. The activation polarization resistance R_{act} is estimated by

$$R_{\text{act}} = \frac{V_{\text{act}}}{i_{\text{FC}}} \tag{11}$$

Subsequently, the voltage of the capacitor V_{C} is given by

$$\frac{dV_{\text{C}}}{dt} = \frac{1}{C_{\text{act}}}\left(i_{\text{FC}} - \frac{V_{\text{C}}}{R_{\text{act}}}\right) \tag{12}$$

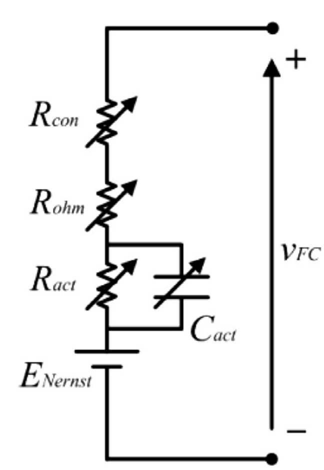

Fig. 2. Equivalent electrical circuit of PEMFC dynamic model.

Accordingly, the output voltage of the single cell based on the simplified dynamic model where V_C, instead of V_{act}, is obtained by

$$v_{cell} = E_{Nernst} - V_C - V_{ohm} - V_{con} \tag{13}$$

The overall stack formed by N cells output voltage is calculated by

$$v_{FC} = N \cdot v_{cell} \tag{14}$$

The parameters and coefficients determined from experimental fittings are listed in Table 1. Fig. 3(a) shows the polarization and power curve comparisons between the proposed model and experimental results. The experimental results were obtained through 200 tests denoted by error bars. The transient responses of the stack output voltage with the stack current input variations are also indicated in Fig. 3(b). The fitting between the model and the real cell shows acceptable accuracy. Therefore, it can be used as a PEMFC control-oriented model with a small degree of freedom. Some deviations occurred at low-current operation condition during the transient operation, but low power is not usually used in actual PEMFC operation.

2.2. DC/DC converter model

The schematics of DC/DC converters are shown in Fig. 4, which includes boost- and buck-type converters with PEMFC equivalent circuit. Each converter comprised a MOSFET switch S, a diode D, an inductor L, and a capacitor C. The external load variable is represented by r_o. After converter conditioning, the PEMFC output voltage v_{FC} can be regulated as the desired load-fed voltage v_o. An inductance large enough to preserve sufficient energy to charge or discharge the output capacitor power is assumed. Hence, the discontinuous conduction operation mode can be neglected.

The state-space form of DC/DC converter is described as

$$\begin{aligned} \dot{\boldsymbol{x}} &= \boldsymbol{A}\boldsymbol{x} + \boldsymbol{B}u + \boldsymbol{G}w \\ y &= \boldsymbol{C}\boldsymbol{x} + \boldsymbol{D}u \end{aligned} \tag{15}$$

where u represents the MOSFET switch location controlled through PWM duty ratio, taking values from the set of {0:1}. y is the output of the system physically calling the load terminal voltage v_o. w is the supply voltage v_{FC} regarded as the system input. $\boldsymbol{A}$, $\boldsymbol{B}$, $\boldsymbol{G}$, $\boldsymbol{C}$, and $\boldsymbol{D}$ are the system dynamic matrices that govern converter characteristics. For boost DC/DC converter

$$\begin{aligned}
\boldsymbol{A}_1 &= \begin{bmatrix} -\frac{1}{L}\left(\frac{R_C \cdot r_o}{R_C + r_o} + R_L\right) & -\frac{1}{L}\cdot\frac{r_o}{R_C + r_o} \\ \frac{1}{C}\cdot\frac{r_o}{R_C + r_o} & -\frac{1}{C}\cdot\frac{1}{R_C + r_o} \end{bmatrix}; \\
\boldsymbol{B}_1 &= \begin{bmatrix} \frac{1}{L}\left(\frac{R_C \cdot r_o}{R_C + r_o}\cdot x_1 + \frac{r_o}{R_C + r_o}\cdot x_2\right) & -\frac{x_1}{C}\cdot\frac{r_o}{R_C + r_o} \end{bmatrix}^T; \\
\boldsymbol{G}_1 &= \begin{bmatrix} \frac{1}{L} & 0 \end{bmatrix}^T; \\
\boldsymbol{C}_1 &= \begin{bmatrix} \frac{R_C \cdot r_o}{R_C + r_o} & \frac{r_o}{R_C + r_o} \end{bmatrix}; \\
\boldsymbol{D}_1 &= \begin{bmatrix} -\frac{R_C \cdot r_o}{R_C + r_o}\cdot x_1 & 0 \end{bmatrix}^T.
\end{aligned} \tag{16}$$

For buck DC/DC converter

$$\begin{aligned}
\boldsymbol{A}_2 &= \begin{bmatrix} -\frac{1}{L}\left(\frac{R_C \cdot r_o}{R_C + r_o} + R_L\right) & -\frac{1}{L}\cdot\frac{r_o}{R_C + r_o} \\ \frac{1}{C}\cdot\frac{r_o}{R_C + r_o} & -\frac{1}{C}\cdot\frac{1}{R_C + r_o} \end{bmatrix}; \\
\boldsymbol{B}_2 &= \begin{bmatrix} \frac{1}{L}\cdot w & 0 \end{bmatrix}^T; \\
\boldsymbol{G}_2 &= [0 \quad 0]^T; \\
\boldsymbol{C}_2 &= \begin{bmatrix} \frac{R_C \cdot r_o}{R_C + r_o} & \frac{r_o}{R_C + r_o} \end{bmatrix}; \\
\boldsymbol{D}_2 &= [0 \quad 0]^T.
\end{aligned} \tag{17}$$

Obviously, controlling a boost converter is more difficult than controlling a buck converter. Moreover, the boost type displays the non-minimum phase phenomenon with the output voltage and current having different phase characteristics [28].

3. PWM control approaches

In this section, three different control approaches are proposed to control the PWM duty ratio. Tables 2 and 3 provide the circuit parameters of the prototype boost and buck converters, respectively. TDC is first mentioned, and two conventional approaches, namely, PIC and MPC, are also introduced to compare the control performances.

3.1. New design based on TDC

A general form of a non-linear time invariant system is described by

$$\dot{\boldsymbol{x}}(t) = \boldsymbol{f}(\boldsymbol{x}(t), t) + \boldsymbol{h}(\boldsymbol{x}(t), t) + \boldsymbol{B}(\boldsymbol{x}(t), t)\boldsymbol{u}(t) + \boldsymbol{d}(t) \tag{18}$$

where $\boldsymbol{x}(t)$ is the state vector, $\boldsymbol{f}(\boldsymbol{x}(t),t)$ is the known dynamics vector, $\boldsymbol{h}(\boldsymbol{x}(t),t)$ is the unknown dynamics vector, $\boldsymbol{B}(\boldsymbol{x}(t),t)$ is the input matrix, $\boldsymbol{u}(t)$ is the control vector, and $\boldsymbol{d}(t)$ is the disturbance vector. Assuming that the state vectors and their derivatives (Eq. (18)), are all observable, the tracking performance satisfies the reference model defined as

$$\dot{\boldsymbol{x}}_{\boldsymbol{m}}(t) = \boldsymbol{A}_{\boldsymbol{m}}\boldsymbol{x}_{\boldsymbol{m}}(t) + \boldsymbol{B}_{\boldsymbol{m}}\boldsymbol{r}(t) \tag{19}$$

where $\boldsymbol{x}_{\boldsymbol{m}}(t)$ and $\boldsymbol{r}(t)$ represent the reference model state vector and input vector, respectively. $\boldsymbol{A}_{\boldsymbol{m}}$ and $\boldsymbol{B}_{\boldsymbol{m}}$ are the system matrices.

Table 1
List of PEMFC parameters used in simulation.

Parameter	Parameter description	Value
T	Stack temperature	333.15 K
P_{H_2}	Partial pressure of hydrogen	2 × 101,325 Pa
P_{O_2}	Partial pressure of oxygen	101325 Pa
$\xi_1, \xi_2, \xi_3, \xi_4, \xi_5$	Cell parametric coefficients	-1.103, 3.48×10^{-3}, 5.8×10^{-5}, -9×10^{-5}, 20
R_C	Constant resistance	2.05×10^{-2} Ω
l	Thickness of the membrane	0.0178 cm
A	Area of the membrane	22.5 cm^2
λ_m	Membrane water content	11
R	Gas constant	8.3145 J $(mol\ K)^{-1}$
F	Faraday constant	96,485 C mol^{-1}
j_{max}	Maximum current density	0.622 A cm^{-2}
N	Number of cell	24

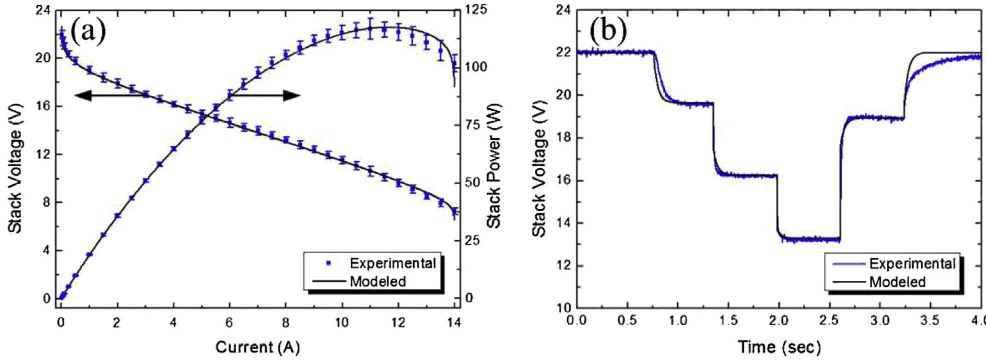

Fig. 3. Comparison between modeled and experimental results: (a) PEMFC polarization and power curves; (b) Transient responses of PEMFC output voltage.

Defining the error as $\boldsymbol{e}(t) = \boldsymbol{x_m}(t) - \boldsymbol{x}(t)$, the error dynamics is given by [32]

$$\dot{\boldsymbol{e}}(t) = \boldsymbol{A_e}\boldsymbol{e}(t) = (\boldsymbol{A_m} + \boldsymbol{K})\boldsymbol{e}(t) \tag{20}$$

where $\boldsymbol{K}$ represents the error feedback gain matrix. The error system is asymptotically stable when the eigen values of $\boldsymbol{A_e}$ are located at the left s- half plane. Combining Eqs. (19) and (20) and rearranging the terms will obtain

$$\boldsymbol{B}(\boldsymbol{x}(t),t)\boldsymbol{u}(t) = -\boldsymbol{f}(\boldsymbol{x}(t),t) - \boldsymbol{h}(\boldsymbol{x}(t),t) - \boldsymbol{d}(t) + \dot{\boldsymbol{x}}_{\boldsymbol{m}}(t) - \boldsymbol{A_e}\boldsymbol{e}(t) \tag{21}$$

If $\boldsymbol{B}(\boldsymbol{x}(t),t)$ is not a square, the pseudo inverse $\boldsymbol{B}^+$ is given by $\boldsymbol{B}^+ = (\boldsymbol{B}^T\boldsymbol{B})^{-1}\boldsymbol{B}^T$. Accordingly, the approximated solution of $\boldsymbol{u}(t)$ is calculated by

$$\boldsymbol{u}(t) = \boldsymbol{B}^+(\boldsymbol{x}(t),t)[-\boldsymbol{f}(\boldsymbol{x}(t),t) - \boldsymbol{h}(\boldsymbol{x}(t),t) - \boldsymbol{d}(t) + \dot{\boldsymbol{x}}_{\boldsymbol{m}}(t) - \boldsymbol{A_e}\boldsymbol{e}(t)] \tag{22}$$

Then, the control input based on TDC law can be calculated by

$$\begin{aligned}\boldsymbol{u}(t) = \boldsymbol{B}^+(\boldsymbol{x},t)[&-\boldsymbol{f}(\boldsymbol{x}(t),t) - \dot{\boldsymbol{x}}(t-T) + \boldsymbol{f}(\boldsymbol{x}(t-T),t-T) \\ &+ \boldsymbol{B}(\boldsymbol{x}(t-T),t-T)\boldsymbol{u}(t-T) + \dot{\boldsymbol{x}}_{\boldsymbol{m}}(t) - \boldsymbol{A_e}\boldsymbol{e}(t)]\end{aligned} \tag{23}$$

More detailed expressions for TDC can be referred from Refs. [32,33]. To apply TDC algorithm to PEMFC-based DC/DC converters, the simplified models can be used without sacrificing the control accuracy. Assuming that the electrical elements are all ideal and very small, i.e., ESR $R_L = R_C = 0$, the state variables are changed as

$$\boldsymbol{x} = [i_{FC} \quad v_o]^T = [x_1 \quad x_2]^T \tag{24}$$

Subsequently, the state space model can be written by substituting ESR = 0 into Eqs. (16) and (17):

$$\begin{aligned}\dot{\boldsymbol{x}} &= \boldsymbol{f}(\boldsymbol{x},t) + \boldsymbol{B}(\boldsymbol{x},t)\boldsymbol{u}(t) + \boldsymbol{d}(t) \\ y &= [0 \quad 1]\boldsymbol{x}\end{aligned} \tag{25}$$

where

$$\begin{aligned}\boldsymbol{f}_1(\boldsymbol{x},t) &= \boldsymbol{f}_2(\boldsymbol{x},t) = \begin{bmatrix} 0 & -\dfrac{1}{L} \\ \dfrac{1}{C} & -\dfrac{1}{C}\cdot\dfrac{1}{r_o}\end{bmatrix}[x_1 \quad x_2]^T; \\ \boldsymbol{B}_1(\boldsymbol{x},t) &= \left[\frac{x_2}{L} \quad -\frac{x_1}{C}\right]^T, \ \boldsymbol{B}_2(\boldsymbol{x},t) = \left[\frac{1}{L}\cdot w \quad 0\right]^T; \\ \boldsymbol{d}_1(t) &= \left[\frac{1}{L}\cdot w \quad 0\right]^T, \ \boldsymbol{d}_2(t) = [0 \quad 0]^T\end{aligned} \tag{26}$$

The subscript 1 represents boost converter and 2 denotes a buck converter for the matrices of $\boldsymbol{f}$, $\boldsymbol{B}$, and $\boldsymbol{d}$.

Then, the following reference variables are chosen:

$$\begin{aligned}x_{m1} &= i_{\mathrm{FC,ref}} = \frac{v_{\mathrm{o,ref}}^2}{r_{\mathrm{o}}\cdot v_{\mathrm{FC}}} \\ x_{m2} &= v_{\mathrm{o,ref}}\end{aligned} \tag{27}$$

The derivative of the reference state variable can simply be denoted as

$$\dot{\boldsymbol{x}}_{\boldsymbol{m}}(t) = 0 \tag{28}$$

Hence, the tracking error and error dynamics are given by

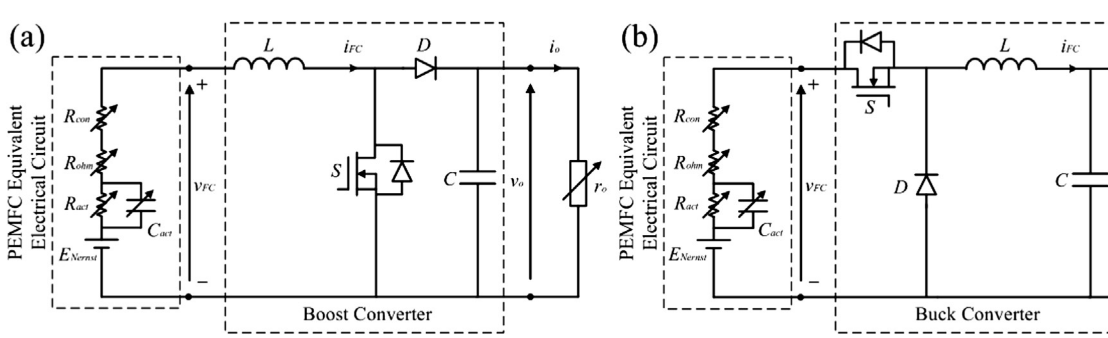

Fig. 4. Schematic circuit of DC/DC converters: (a) boost converter; (b) buck converter.

Table 2
List of parameters for DC/DC boost converter.

Parameter	Parameter description	Value
C	Capacitance	200 μF
L	Inductance	500 μH
R_C	ESR of capacitor	30 mΩ
R_L	ESR of inductor	30 mΩ
PWM frequency	PWM frequency	30 kHz

Table 3
List of parameters for DC/DC buck converter.

Parameter	Parameter description	Value
C	Capacitance	1000 μF
L	Inductance	1000 μH
R_C	ESR of capacitor	30 mΩ
R_L	ESR of inductor	30 mΩ
PWM frequency	PWM frequency	30 kHz

$$\boldsymbol{e}(t) = \boldsymbol{x_m}(t) - \boldsymbol{x}(t) \tag{29a}$$

$$\dot{\boldsymbol{e}}(t) = \boldsymbol{K}[\boldsymbol{x_m}(t) - \boldsymbol{x}(t)] \tag{29b}$$

A canonical form was presented to model the TDC reference model in Ref. [37]. The output voltage is the main control purpose. Moreover, this study only used voltage terms to construct the controller. Therefore, the control input of the boost converter is obtained as

$$\begin{aligned} u(t) &= \frac{L}{v_o(t)}\left[\frac{v_o(t)}{L} - \hat{\dot{i}}_{FC}(t-T) - \frac{v_o(t-T)}{L} + \frac{v_o(t-T)}{L}u(t-T) - A_e e(t)\right] \\ &= \frac{v_o(t) - L\hat{\dot{i}}_{FC}(t-T) + v_o(t-T)[u(t-T)-1] - LK\left[v_{o,ref} - v_o(t)\right]}{v_o(t)} \end{aligned} \tag{30}$$

The control input of the buck converter is calculated by

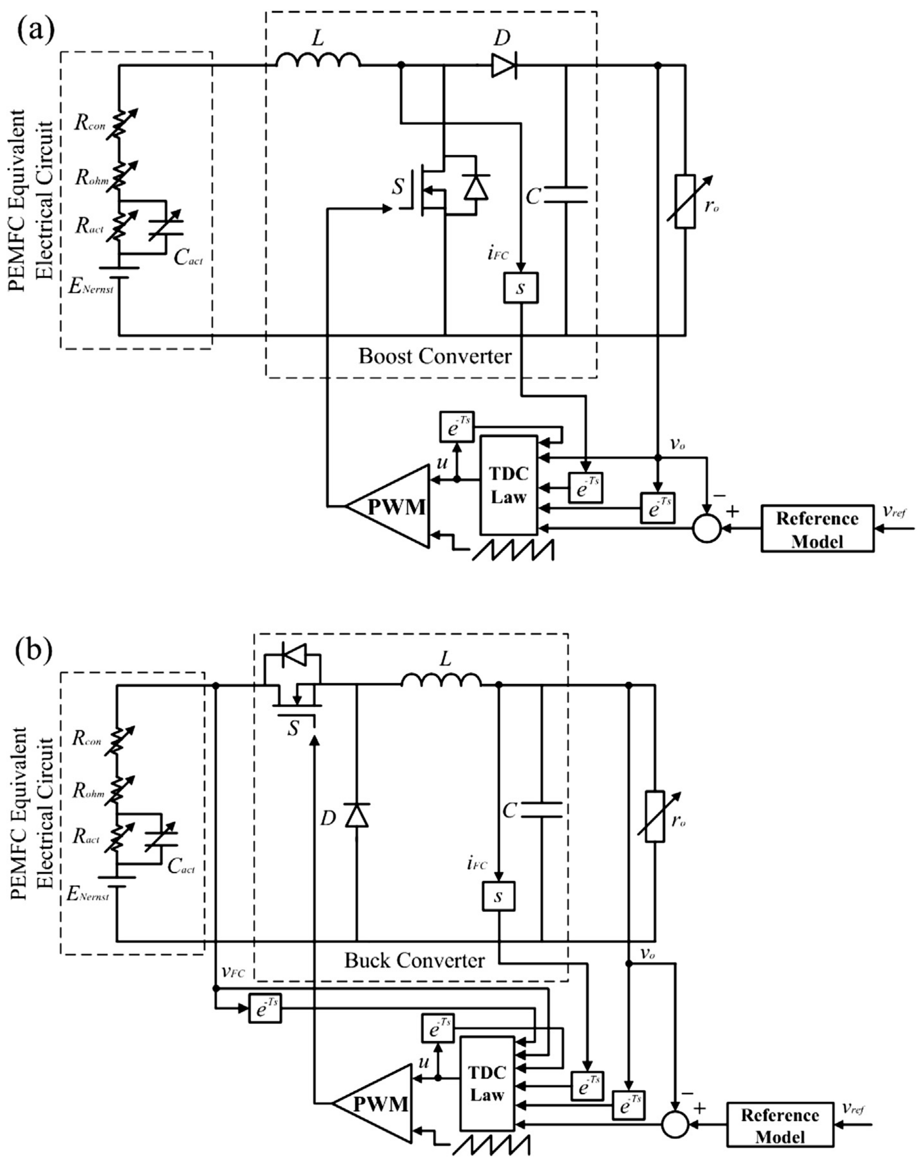

Fig. 5. Block diagram of TDC for PEMFC-based DC/DC converters: (a) with boost converter; (b) with buck converter.

$$
\begin{aligned}
u(t) &= \frac{L}{v_{FC}(t)}\left[\frac{v_o(t)}{L} - \hat{\dot{i}}_{FC}(t-T) - \frac{v_o(t-T)}{L} + \frac{v_{FC}(t-T)}{L}u(t-T) - A_e e(t)\right] \\
&= \frac{v_o(t) - L\hat{\dot{i}}_{FC}(t-T) + v_{FC}(t-T)u(t-T) - v_o(t-T) - LK\left[v_{o,ref} - v_o(t)\right]}{v_{FC}(t)}
\end{aligned}
\tag{31}
$$

where is the numerical derivative of PEMFC current, and K is a negative constant to ensure that error dynamics are convergent. In boost and buck converters, K equals to -0.8 and -0.1, respectively. To select the suitable time delay T, which usually has same time period as the sampling time T_s or its integer multiple, a simple polynomial characteristic equation is derived using a second-order Padé approximation. Time delay T is chosen as $T = T_s = 1$ ms in our study. The TDC law-governed PEMFC-based DC/DC converter control scheme is shown in Fig. 5.

3.2. Conventional design based on PIC and MPC

To test the superiority of TDC performance, PIC and MPC are chosen with the same control specification utilized in the TDC design. The transient specifications are as follows: response time, <0.2 s; and small percentage of overshoot. Both PIC and MPC are designed based on the small-signal averaging models obtained from the linearization of Eqs. (15)–(17). For the boost converter [19]

$$
\frac{\hat{V}_o(s)}{\hat{U}(s)} = \frac{V_o(1-U_o)}{LC}\cdot\frac{\left(1-\frac{L}{R_o(1-U_o)^2}s\right)\left(1+\frac{R_C}{R_o}+R_C C s\right)}{\frac{R_L+R_C(1-U_o)+R_o(1-U_o)^2}{R_o LC} + \frac{R_o C(R_L+R_C(1-U_o))+L}{R_o LC}s + s^2}
\tag{32}
$$

where V_o and U_o are the nominal values of voltage and PWM duty ratio, respectively. The nominal operation point for boost converter is chosen by considering PEMFC-rated power range of approximately (14.6 V, 6 A), which is given by $V_{FC} = 14.6$ V, $V_o = 24$ V, and $U_o = 0.392$. The transfer function at the nominal operation is obtained as

$$
\frac{\hat{V}_o(s)}{\hat{U}(s)} = \frac{-0.1801s^2 - 2.9279\times10^4 s + 1.4659\times10^8}{s^2 + 8.5694\times10^2 s + 3.7700\times10^6}
\tag{33}
$$

For the buck converter [19]

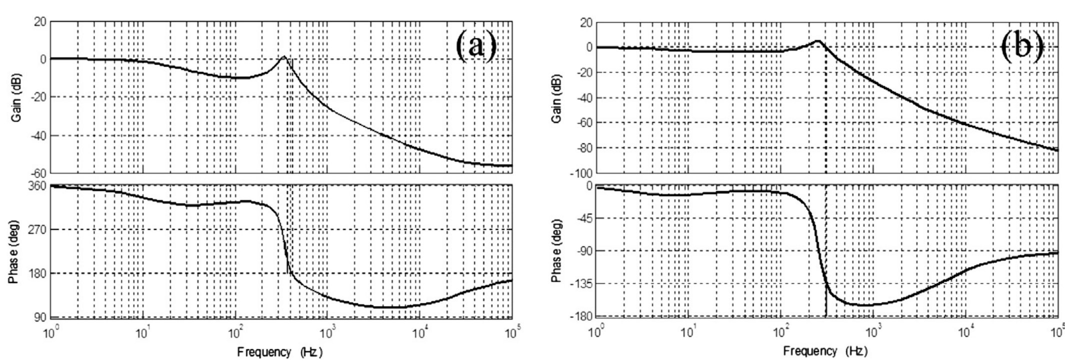

Fig. 6. Frequency responses of PIC compensated systems: (a) boost converter; (b) buck converter.

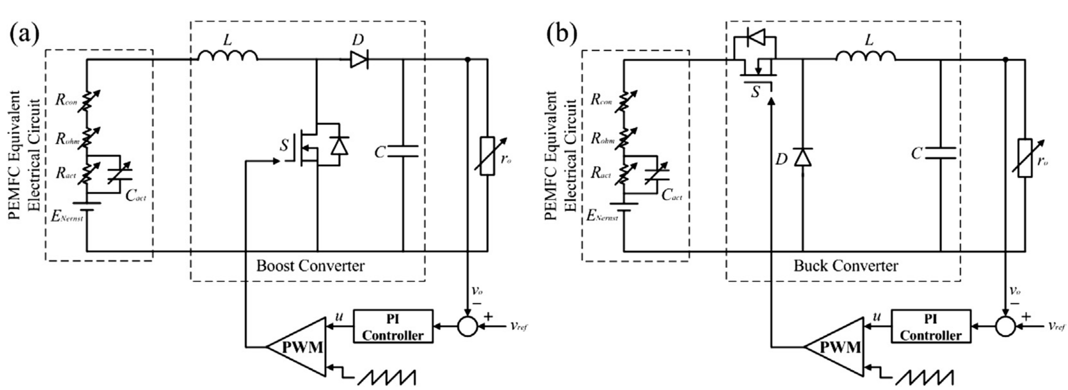

Fig. 7. Block diagram of PIC for PEMFC-based DC/DC converters: (a) with boost converter; (b) with buck converter.

Table 4
List of MPC parameters.

Parameter	Parameter description	Boost DC/DC converter	Buck DC/DC converter
P	Prediction horizon	10	14
M	Control horizon	1	2
φ	Output weighting	1	0.5
γ	Input weighting	1	1
$v_{o,min}$	Minimum ripple voltage at nominal	18 V	10 V
$i_{FC,min}$	Minimum ripple current at nominal	4.5 A	2 A
$v_{o,max}$	Maximum ripple voltage at nominal	30 V	15 V
$i_{FC,max}$	Maximum ripple current at nominal	12.5 A	14 A
Δu_{min}	Minimum control action	−0.5	−0.5
Δu_{max}	Maximum control action	0.5	0.5

$$\frac{\widehat{V}_o(s)}{\widehat{U}(s)} = \frac{V_o}{U_o} \cdot \frac{(1 + R_C C s)}{1 + \left(\frac{L}{R_L + R_o} + R_C C + \frac{R_L R_o}{R_L + R_o} C\right)s + \frac{R_C + R_o}{R_L + R_o} L C s^2} \tag{34}$$

with the nominal operation point chosen as $V_{FC} = 14.6$ V, $V_o = 12$ V, and $U_o = 0.822$. The transfer function at the nominal operation is

$$\frac{\widehat{V}_o(s)}{\widehat{U}(s)} = \frac{4.3796 \times 10^{-4} s + 14.5985}{1.0 \times 10^{-6} s^2 + 5.5217 \times 10^{-4} s + 1} \tag{35}$$

3.2.1. PIC design

In conjunction with test results, a suitable PIC is designed for the boost converter

$$G_c(s) = 0.0083 + \frac{3.3}{s}, \tag{36}$$

and for buck converter

$$G_c(s) = 0.11 + \frac{6.05}{s}. \tag{37}$$

The bode plots for the PIC-compensated systems are shown in Fig. 6. For the boost converter, the phase margin is 29.5° at the gain crossover frequency of approximately 373 Hz. By contrast, the phase margin is 45.8° at gain crossover frequency of approximately 309 Hz for the buck converters. The control diagram is shown in Fig. 7.

3.2.2. MPC design

The main process of MPC involves the calculation of a series of control actions of PWM duty ratio based on DC/DC converter model predictions to minimize the error between output voltage and setpoint value. The obtained control sequence calculates new predictions and further updates the manipulated variables. The number of new predictions is called prediction horizon P, and the updated control sequence number is called control horizon M, where $P > M$. The linearized model plants of DC/DC converters with controlled auto-regressive integrated moving average predictor (CARIMA) [40] are used to predict the future outputs. CARIMA is given by

$$A\left(z^{-1}\right) \cdot \tilde{y}(k) = B\left(z^{-1}\right) \cdot u(k-1) + D\left(z^{-1}\right) \cdot w(k) + \frac{1}{\Delta} \cdot C\left(z^{-1}\right) \cdot e(k) \tag{38}$$

where $\tilde{y}(k)$, $u(k-1)$, $w(k)$, and $e(k)$, are the plant output prediction, manipulated variable, system disturbance, and noise at time instant k, respectively. The operator Δ is defined by $\Delta = 1 - z^{-1}$. Moreover, through model predication, the manipulated variable is the solution of the constrained optimization problem and subjects the cost function formulated by

$$\begin{gathered} J = \sum_{j=1}^{P} \varphi_j[\tilde{y}(k+j|k) - r(k+j)]^2 + \sum_{j=1}^{M} \gamma_j[u(k+j-1)]^2 \\ y_{min} \le \tilde{y}(k+j|k) \le y_{max} \\ u_{min} \le u(k+j|k) \le u_{max} \\ \Delta u_{min} \le \Delta u(k+j|k) \le \Delta u_{max} \end{gathered} \tag{39}$$

Quadratic programming problem can be solved by minimizing the cost function

$$u^* = \operatorname{argmin} J(u, r, x) \tag{40}$$

where $\tilde{y}(k+j|k) - r(k+j)$ denotes the output error of predicted time instant $k+j$ based on the s plant information of time instant k, Δu is the control action, and u^* is the optimal control input. ϕ_j and γ_j represent output weight factor and manipulated variable weigh factor, respectively. The constraints in Equation (39) are made according to the physical limitations and performance specification, for example, the maximum operation voltage of capacitor and maximum ripple voltage used in the boost converter. The MPC parameters are obtained through heuristics and are given in Table 4. Fig. 8 shows the disturbance rejection performance of MPC under the prediction horizon P and the control horizon M. The horizons can be found using the closed-loop prediction of the

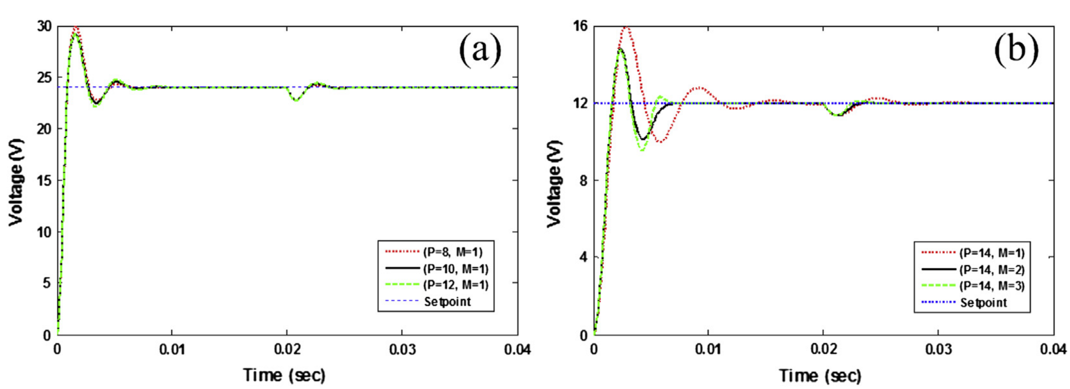

Fig. 8. Prediction horizon P and control horizon M tuning under step load injection for MPC: (a) boost converter; (b) buck converter.

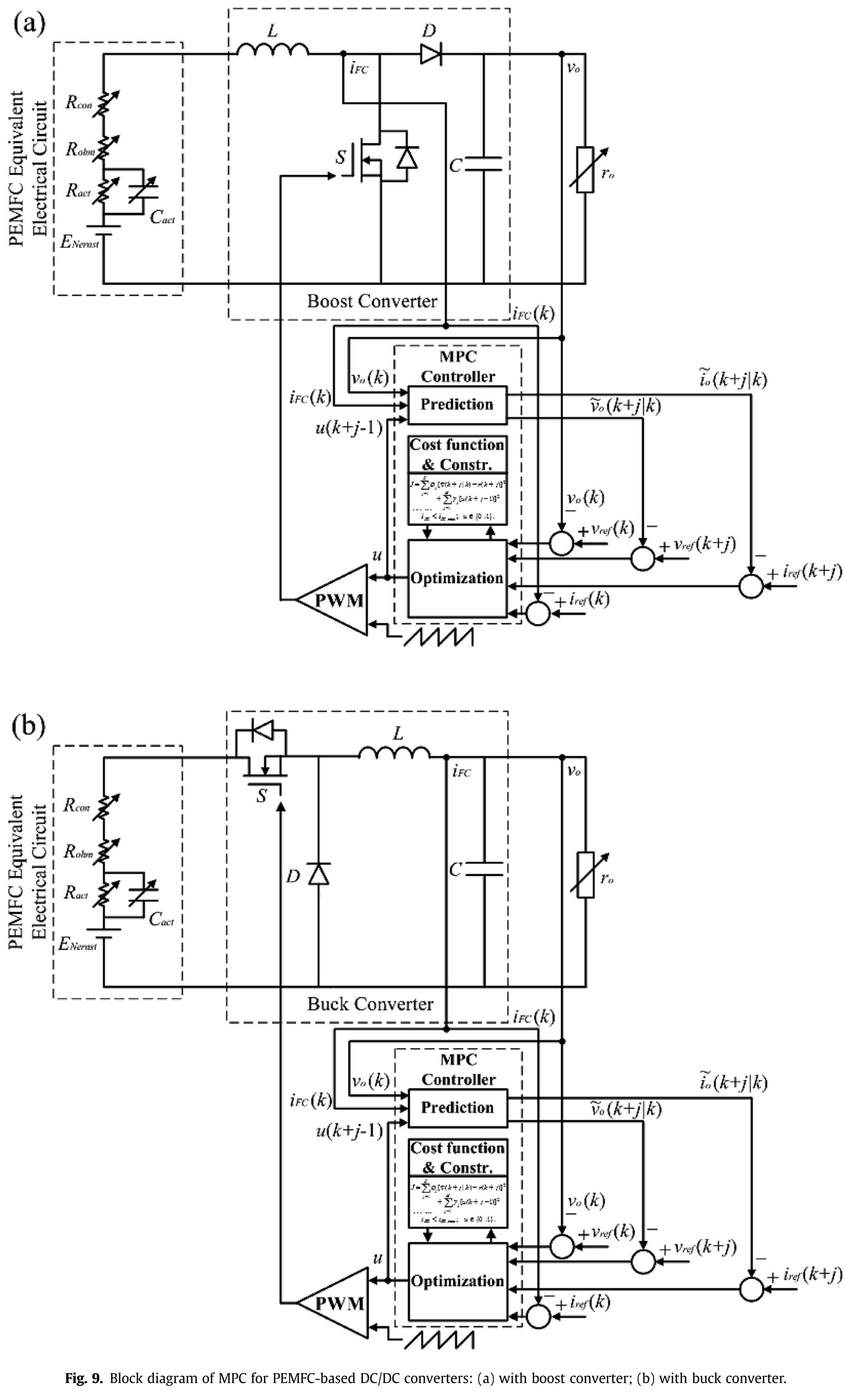

Fig. 9. Block diagram of MPC for PEMFC-based DC/DC converters: (a) with boost converter; (b) with buck converter.

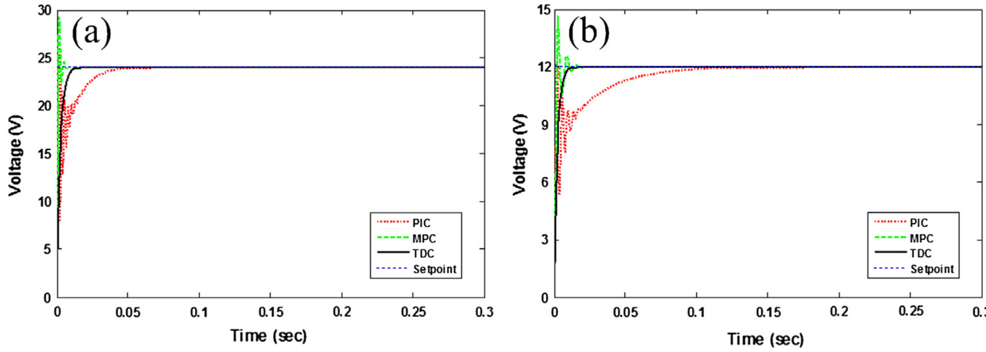

Fig. 10. Steady-state input condition results of PEMFC-based DC/DC converters without external applied load: (a) boost converter case; (b) buck converter case.

output and its sensitivity [41]. The overall MPC control system of the converter is exhibited in Fig. 9.

4. Numerical simulation results and experimental validation

The numerical simulation results and experimental validations are presented in this section, based on the design parameters in Tables 2 and 3. The main purpose of the present study is to design and test the proposed control techniques for PEMFC-fed DC/DC converters. Tracking 24 V for boost converter and 12 V for buck converter are chosen as the control specifications for the simulation and experimental implementation. The maximum working power of 100 W for the converter is chosen to avoid concentration loss of PEMFC and to protect the PEMFC. Simulations are performed first under MATLAB/Simulink platform, which depends on the designed control schematic diagrams shown in Figs. 5, 7 and 9. Real-time experiments were also performed with NI DAQ system with LabVIEW to validate the effectiveness of the proposed control.

4.1. Results of numerical simulation

The results of the three control methods under steady-state input conditions without externally applied load are shown in Fig. 10. Each controller shows desired control performance, i.e., the settling time is less than 0.2 s, and tracking error is within the specified level. Moreover, TDC shows the best control performance with the fastest response and without overshoot in both boost and buck converters, whereas PIC shows sluggish response, and MPC exhibits large overshoot. An abrupt external load change is also applied to determine the disturbance rejection ability. Even in the presence of an external disturbance, DC/DC converters are still required to supply the constant voltage accurately and promptly to the secondary power buses. The results of the boost converter under abrupt external disturbance engagement are shown in Fig. 11. TDC shows the most robust tracking performance against the other controllers. Immediately after the introduction of the disturbance, TDC vanishes DC/DC output voltage ripple. Hence, error diminishes rapidly. For example, when the maximum disturbance occurs, TDC settling time is just approximately 0.01 s with 4.6 V overshoot. However, MPC settling time is approximately 0.04 s with 10.8 V overshoot and that of PIC is approximately 0.2 s with 9.6 V overshoot. Simultaneously, PEMFC shows the most stable stack voltage response under TDC, which guarantees a stable fuel cell operation.

TDC shows the best control performance (Fig. 12(c)), among the three controllers for PEMFC-fed DC/DC buck converter in terms of response time, overshoot, and ripples. MPC shows faster response in steady-state operation. However, MPC has higher overshoot and larger ripples in the presence of a disturbance. The ripples may impact the PEMFC stack voltage oscillations as shown in Fig. 12(b), which may degrade the fuel cell performance in long-term usage. By contrast, the disadvantage of PIC is its sluggish response in the presence of a disturbance. For example, at maximum applied load, PIC requires approximately 0.2 s to track the setpoint. The simulation results reveal that TDC shows the most excellent transient responses for PEMFC-fed boost and buck DC/DC converter application.

4.2. Experimental validation

An experimental test rig is constructed using NI PCI-6229 DAQ board, SCXI-1313A signal conditioner, H-100 PEMFC, DC/DC boost and buck converters, electronic load, and TDS3034B series digital phosphor oscilloscope (Fig. 13). PCI-6229, a data acquisition device with 32 analog inputs (16 bits, 250 kS s^{-1}) and 4 analog outputs (16 bits, 833 kS s^{-1}), provides optimized functionality for cost-sensitive applications [42]. SCXI-1313A is used for high-voltage attenuation and AC/DC coupling. NI LabVIEW system provides a widely used graphic user design interface, which is easy to program with various and friendly hardware I/O ports. Therefore, real-time measurement and control for PEMFC converter systems are easily implemented. The voltage and current sensing are recorded through oscilloscope and LabVIEW system. The current is transformed to voltage through a Hall-effect sensor, WCS2705, or WCS2720.

Fig. 14 shows the response of the starting period of the PEMFC-fed DC/DC boost converter, where the five fluctuated PEMFC voltage loops are caused by H-100 PEMFC built-in start mode. H-100 PEMFC has no relation with the DC/DC converter control effect. Large fluctuations caused by PEMFC "short circuit" operation mode at the start period that may increase stack voltage [38]. At this time, TDC shows a rapid response (<0.1 s) with smaller overshoots (maximum overshoot of 3 V) to track the setpoint, whereas MPC shows the worst performance with large overshoots of approximately 7 V.

The disturbance rejection ability was tested through abrupt external load engagement. The results of the boost converter controlled by PIC, MPC, and TDC are shown in Fig. 15(a)–(c), respectively. TDC exhibits the best transient performance in considering the response time and overshoot, whereas MPC shows corresponding values of 0.2 s and 4.1 V, and those of PIC are 0.3 s and 7 V under maximal load. Fig. 16(a)–(c) shows the response of disturbance rejection ability for the DC/DC buck converter under sudden external load change. TDC displays the

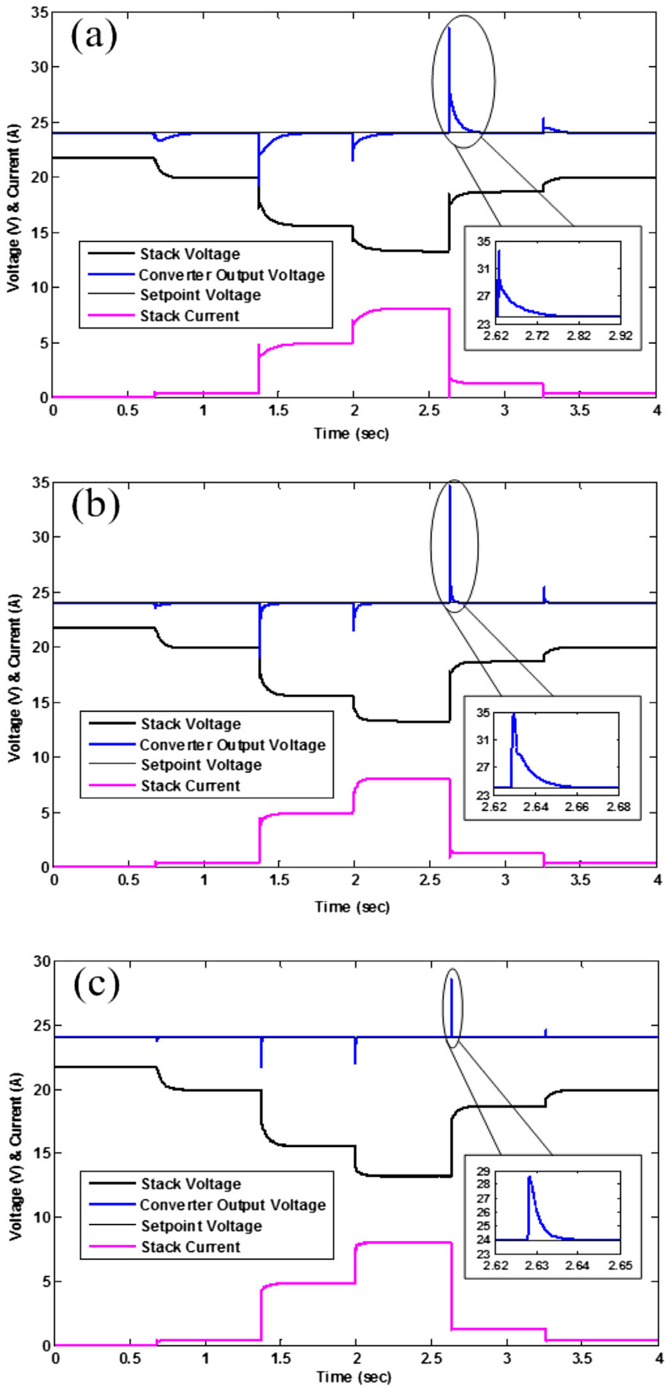

Fig. 11. Response of step load applied to PEMFC-based DC/DC boost converter: (a) with PIC; (b) with MPC; (c) with TDC.

best performance against PIC and MPC. Considering the results presented in Figs. 15 and 16, TDC is the most suitable control technique among the three controllers for PEMFC-fed DC/DC converters. Moreover, a ramped load is applied to the converters to examine the operation range of the converter. The tests are implemented on the boost converter using PIC and TDC only. PIC and TDC almost showed similar control results (Fig. 17). Both have quick response times and small ripples, which indicate that both controllers are useful in regulating the output voltage for the variation in ramp load. TDC result shows much faster transient dynamics for boost converter; however, better transient response cannot be obtained for buck converter even TDC is applied. This is because boost converter has the non-minimum phase characteristics.

The tracking errors for start mode and step-load change operation mode are calculated by root mean square error (RMSE). RMSE comparisons among PIC, MPC, and TDC are listed in Table 5. TDC shows the minimum errors to track the setpoint in boost and buck converters under different working conditions.

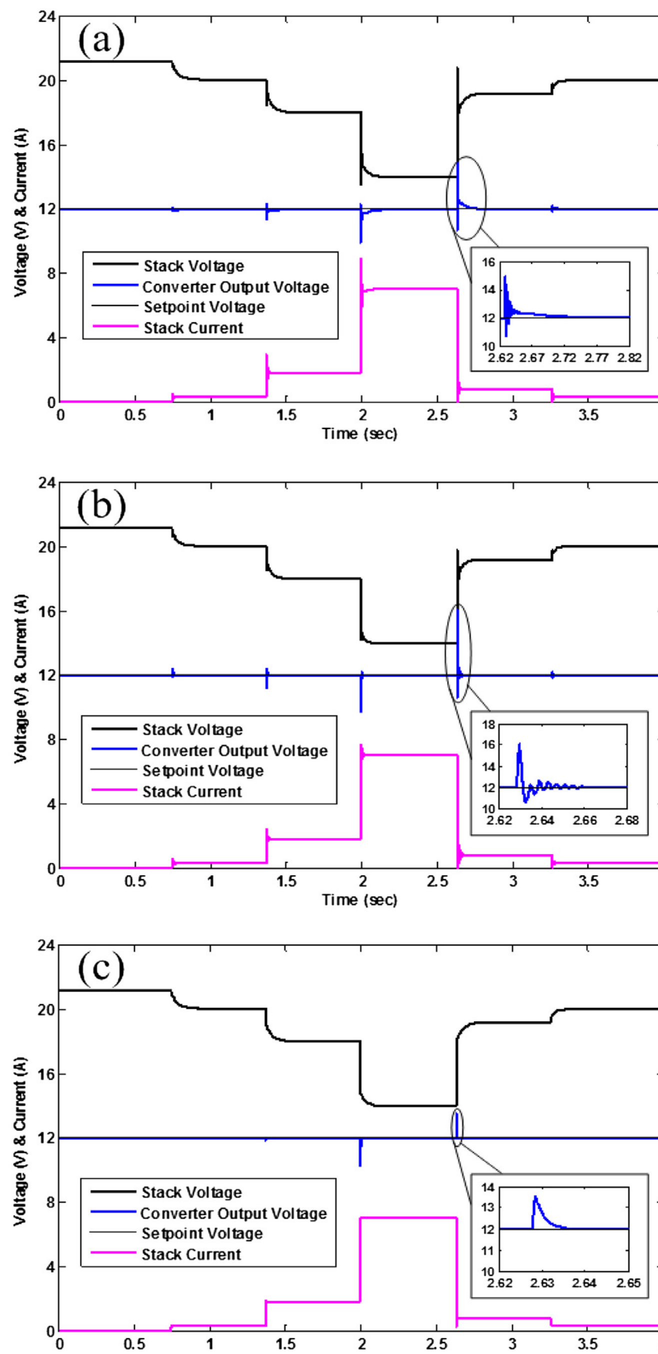

Fig. 12. Response of step load applied to PEMFC-based DC/DC buck converter: (a) with PIC; (b) with MPC; (c) with TDC.

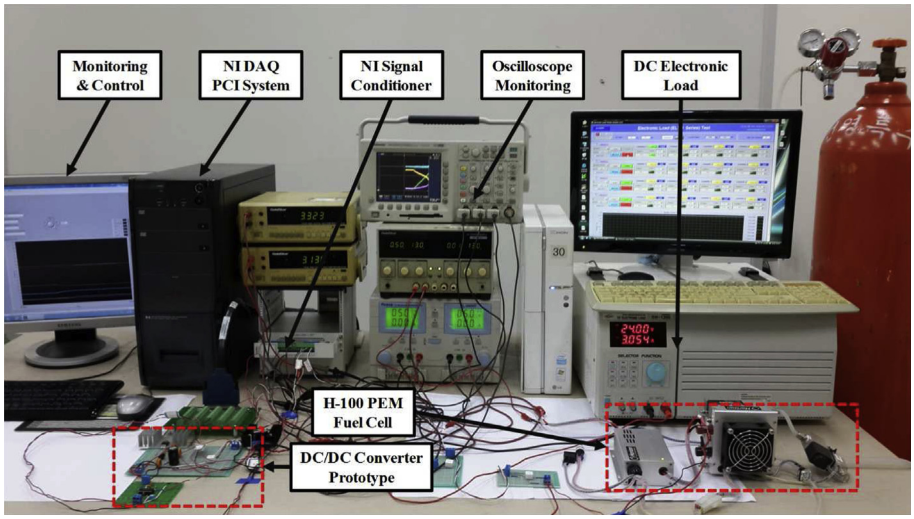

Fig. 13. Picture of an experimental test rig.

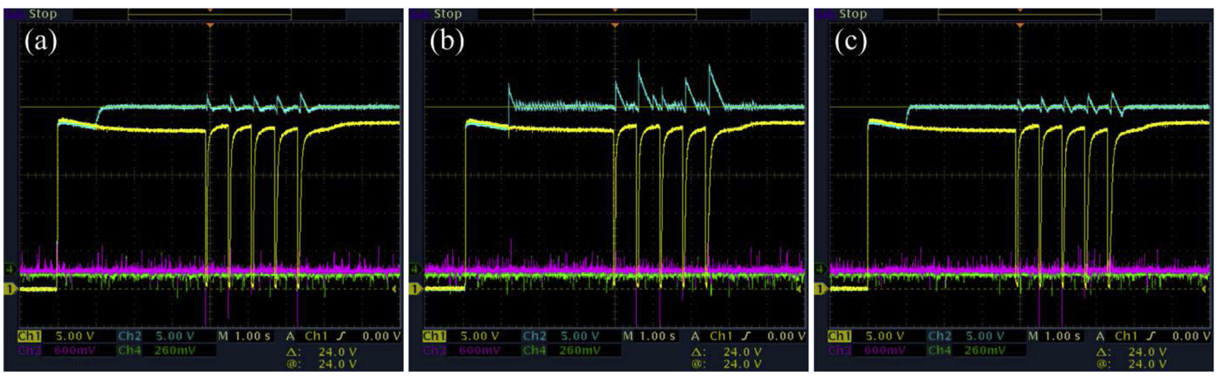

Fig. 14. Experimental results of PEMFC-based DC/DC boost converter with start operation: (a) with PIC; (b) with MPC; (c) with TDC. Notes on the oscilloscope: Channel 1 is the PEMFC stack voltage; Channel 2 is the DC/DC converter output voltage; Channel 3 is the transformed voltage of PEMFC stack current; Channel 4 is the transformed voltage of load current.

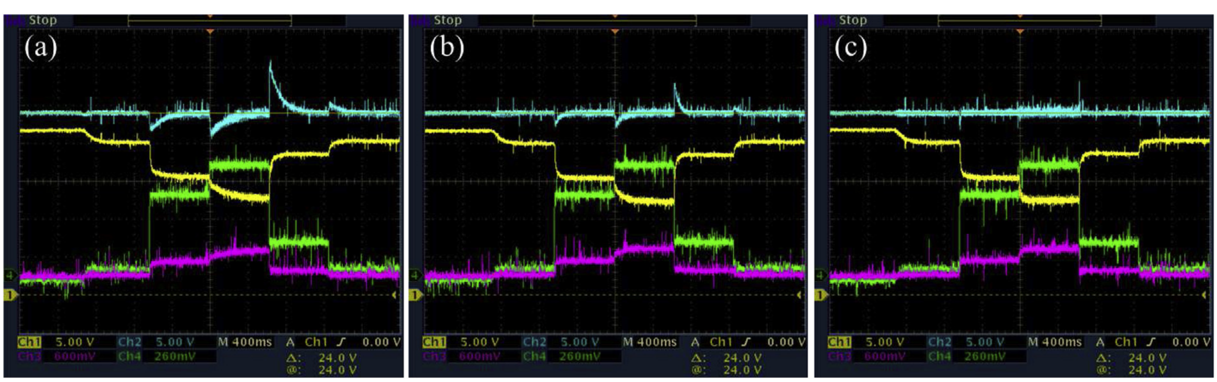

Fig. 15. Experimental results of PEMFC-based DC/DC boost converter step load injection: (a) with PIC; (b) with MPC; (c) with TDC. Notes on the oscilloscope: Channel 1 is the PEMFC stack voltage; Channel 2 is the DC/DC converter output voltage; Channel 3 is the transformed voltage of PEMFC stack current; Channel 4 is the transformed voltage of load current.

5. Conclusions

This study introduces a robust control technique for PWM-regulated DC/DC converters used for PEMFC application. The study focuses on the PEMFC-fed PWM DC/DC converter controller to supply both constantly high (boost action) and low (buck action) DC voltage to the subsequent power link. PEMFC dynamics is modeled through equivalent electrical circuits with a variable capacitor, and linearized DC/DC converter models are added for full control. Based on the control-oriented full model, including PEMFC and two DC/DC converters, three control techniques, namely, TDC, MPC, and PIC, are designed and simulated using MATLAB/Simulink. The simulation results reveal that TDC is the most preferable control technique for boost and buck DC/DC converters in PEMFC application. TDC provided a stable and fast DC link voltage. Boost and buck DC/DC converters are constructed and connected to the

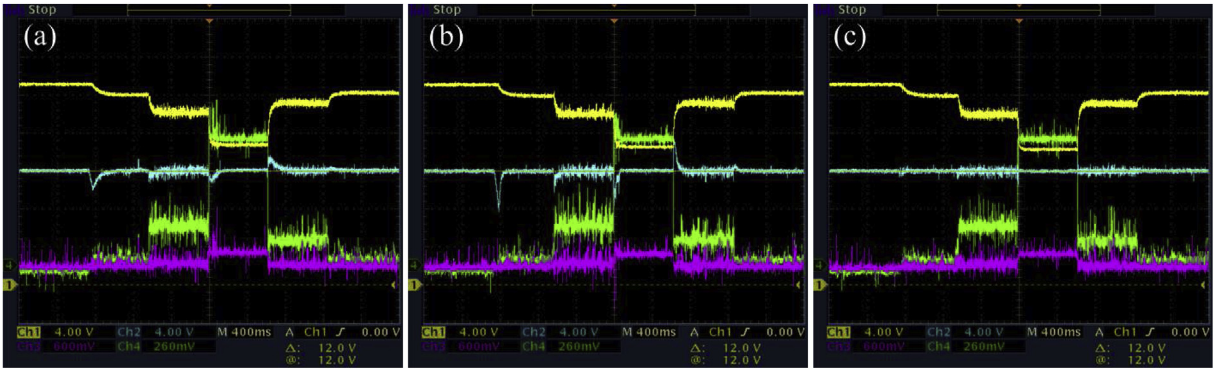

Fig. 16. Experimental results of PEMFC-based DC/DC buck converter step load injection: (a) with PIC; (b) with MPC; (c) with TDC. Notes on the oscilloscope: Channel 1 is the PEMFC stack voltage; Channel 2 is the DC/DC converter output voltage; Channel 3 is the transformed voltage of PEMFC stack current; Channel 4 is the transformed voltage of load current.

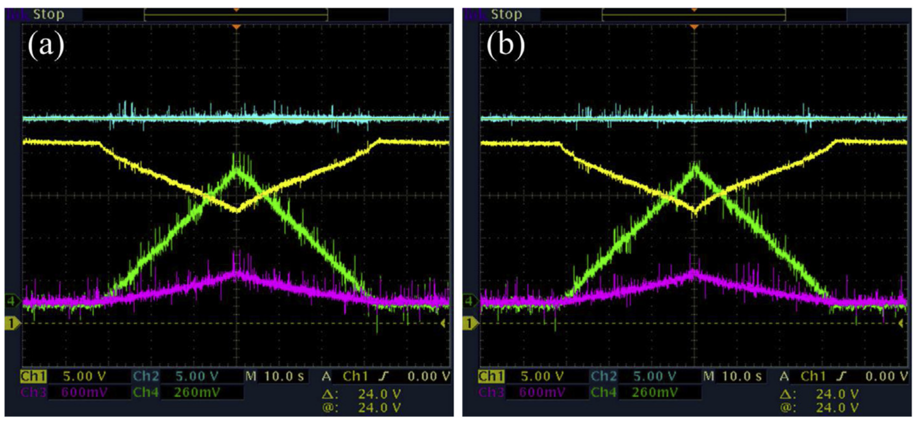

Fig. 17. Experimental results of PEMFC-based DC/DC boost converter ramp load injection: (a) with PIC; (b) with TDC. Notes on the oscilloscope: Channel 1 is the PEMFC stack voltage; Channel 2 is the DC/DC converter output voltage; Channel 3 is the transformed voltage of PEMFC stack current; Channel 4 is the transformed voltage of load current.

Table 5
Results of RMSE with experimental results.

Operation mode	PIC	MPC	TDC
Start mode with boost converter	7.5825	7.9273	7.5977
Start mode with buck converter	5.4204	5.3570	5.0889
Step load mode with boost converter	0.9733	0.4357	0.2844
Step load mode with buck converter	0.3195	0.4840	0.1384

H-100 PEMFC to prove the efficacy of the TDC experimentally. NI DAQ LabVIEW system is utilized as a real-time control, and a series of the tests are implemented to compare the effects of the three controls. The experimental results showed the superiority of TDC performance to those of PIC and MPC in providing stable and fast DC power link, even when the input voltage or external output load varies. Its relatively easy design process is another advantage of using TDC because tuning its parameters is much simpler than those of PIC and MPC. The proposed topology and control approach can be utilized for other power source-based fed converters, such as photovoltaic cells, super capacitors, and batteries.

Acknowledgment

This work was supported by the National Research Foundation of Korea (NRF) funded by the Ministry of Education (2013-10005339).

References

[1] V. Mehta, J.S. Cooper, J. Power Sources 114 (1) (2003) 32–53.
[2] K. Simmons, Y. Guezennec, S. Onori, J. Power Sources 246 (2014) 736–746.
[3] A. Emmadi, S.S. Williams, A. Khaligh, IEEE Trans. Power Electron. 21 (3) (2006) 57–577.
[4] B. Zhou, W. Huang, Y. Zong, A. Sobiesiak, J. Power Sources 155 (2) (2006) 190–202.
[5] Z.H. Wang, C.Y. Wang, K.S. Chen, J. Power Sources 94 (1) (2001) 40–50.
[6] Y. Wang, C.Y. Wang, J. Power Sources 147 (1–2) (2005) 148–161.
[7] T.V. Nguyen, R.E. White, J. Electrochem. Soc. 140 (8) (1993) 2178–2186.
[8] S.Y. Choe, J.G. Lee, J.W. Ahn, S.H. Baek, J. Power Sources 164 (2) (2007) 614–623.
[9] J.M. Correa, F.A. Farret, L.N. Canha, M.G. Simoes, IEEE Trans. Ind. Electron. 51 (5) (2004) 1103–1112.
[10] W.J. Yang, H.Y. Wang, Y.B. Kim, Int. J. Energy Res. 37 (11) (2013) 1339–1348.
[11] T. Bjazic, Z. Ban, M. Milanovic, J. Power Sources 198 (15) (2012) 203–217.
[12] D. Giaouris, F. Stergiopoulos, C. Ziogou, D. Ipsakis, S. Banerjee, B. Zahawi, V. Pickert, S. Voutetakis, S. Papadopoulou, Int. J. Hydrogen Energy 37 (23) (2012) 18205–18215.
[13] J.K. Kuo, C.F. Wang, Int. J. Hydrogen Energy 36 (18) (2011) 11846–11855.
[14] G. Marsala, M. Pucci, G. Vitale, M. Cirrincione, A. Miraoui, Appl. Energy 86 (36) (2009) 2192–2203.
[15] Y.B. Kim, S.J. Kang, Int. J. Hydrogen Energy 35 (16) (2010) 8792–8803.
[16] C. Wang, M.H. Nehrir, S.R. Shaw, IEEE Trans. Energy Convers. 20 (2) (2005) 442–451.
[17] R.D. Middlebrook, Proc. IEEE 76 (4) (1988) 343–354.
[18] F.H.F. Leung, P.K.S. Tam, C.K. Li, IEEE Trans. Ind. Electron. 38 (1) (1991) 65–71.
[19] L. Guo, J.Y. Hung, R.M. Nelms, IEEE Trans. Ind. Electron. 56 (6) (2009) 2237–2248.
[20] H. Fujioka, C.Y. Kao, S. Almer, U. Jonsson, Automatica 45 (8) (2009) 1808–1818.
[21] C. Olalla, R. Leyva, I. Queinnec, D. Maksimovic, IEEE Trans. Power Electron. 27 (6) (2012) 3006–3019.

[22] Y.B. Shtessel, R.S. Ashok, in: IEEE Conference on Decision and Control and European Control Conference (CDC-ECC 2011), Orlando, 12–15 December 2011, pp. 8261–8266.
[23] F.A. Inthamoussou, R.J. Mantz, H.D. Battista, J. Power Sources 205 (2012) 281–289.
[24] F. Zenith, S. Skogestad, J. Process Control 17 (4) (2007) 333–347.
[25] S.C. Tan, Y.M. Lai, C.K. Tse, IEEE Trans. Ind. Electron. 55 (3) (2008) 1160–1174.
[26] R.J. Wai, C.Y. Lin, IEEE Trans. Ind. Electron. 57 (11) (2010) 3780–3792.
[27] T. Geyer, G. Papafotiou, M. Morari, IEEE Trans. Control Syst. Technol. 16 (6) (2008) 1112–1124.
[28] S. Mariethoz, S. Almer, M. Baja, A.G. Beccuti, D. Patino, A. Wernrud, J. Buisson, H. Cormerais, T. Geyer, H. Fujioka, U.T. Jonsson, C.Y. Kao, M. Morari, G. Papafotiou, A. Rantzer, P. Riedinger, IEEE Trans. Control Syst. Technol. 18 (5) (2010) 1126–1145.
[29] A.S. Samosir, A.H.M. Yatim, IEEE Trans. Ind. Electron. 57 (10) (2010) 3468–3473.
[30] R.J. Wai, L.C. Shih, IEEE Trans. Power Electron. 27 (4) (2012) 2104–2115.
[31] M. Bensaada, A.B. Stambouli, Int. J. Electr. Power Energy Syst. 53 (2013) 761–773.
[32] K. Youcef-Toumi, U. Ito, in: American Control Conference, Atlanta, 15–17 June 1988, pp. 904–913.
[33] K. Youcef-Toumi, S. Reddy, J. Dyn. Syst. Meas. Control 114 (4) (1992) 544–555.
[34] J. H. Jung, P. H. Chang, S. H. Kang, in: American Control Conference, New York, 9–13 July 2007, pp. 5995–6002.
[35] P.H. Chang, J.W. Lee, IEEE Trans. Control Syst. Technol. 4 (1) (1996) 2–10.
[36] Y.X. Wang, D.J. Xuan, Y.B. Kim, Int. J. Hydrogen Energy 38 (30) (2013) 13381–13392.
[37] Y.X. Wang, D.H. Yu, Y.B. Kim, IEEE Trans. Ind. Electron 61 (9) (2014) 4829–4837, http://dx.doi.org/10.1109/TIE.2013.2290764.
[38] Horizon Fuel Cell Technologies Inc., H-100 Fuel Cell Stack User Manual, http://www.horizonfuelcell.com/#!h-series-stacks/c52t.
[39] Y. Zhang, B. Zhou, J. Power Sources 196 (20) (2011) 8413–8423.
[40] A. Arce, A.J. del Real, C. Bordons, D. Ramirez, IEEE Trans. Ind. Electron. 57 (6) (2010) 1892–1905.
[41] A. Al-Ghazzawi, E. Ali, A. Nouh, E. Zafiriou, J. Process Control 11 (3) (2001) 265–284.
[42] http://sine.ni.com/nips/cds/view/p/lang/en/nid/14136.